3D local residual stress and orientation gradients near graphite nodules in ductile cast iron

Y.B. Zhang [1*], T. Andriollo [2], S. Fæster [1], W. Liu [3], J. Hattel [2], R. Barabash [4]

[1] Section for Materials Science and Advanced Characterization, Department of Wind Energy, Technical University of Denmark, Risø Campus, Roskilde 4000, Denmark

[2] Department of Mechanical Engineering, Technical University of Denmark, DK-2800 Kgs. Lyngby, Denmark

[3] Advanced Photon Source, Argonne National Laboratory, Argonne, Illinois 60439-4800, USA

[4] Materials Science & Technology Division, Oak Ridge National Laboratory, P.O. Box 2008, Oak Ridge, Tennessee 37831-6118, USA

[*] Corresponding author. Address: Frederiksborgvej 399, Roskilde 4000, Denmark. Phone: +45 46775876. E-mail: yubz@dtu.dk

Abstract:

A synchrotron technique, differential aperture X-ray microscopy (DAXM), has been applied to characterize the microstructure and analyze the local residual elastic strain fields around graphite nodules embedded in ferrite matrix grains in a ductile cast iron. Compressive residual elastic strains are observed with a maximum strain of ~ 6.5-8 × 10^{-4} near the graphite nodules extending into the matrix about 20 µm, where the elastic strain is near zero. The experimental data are compared with strain gradient calculated by a finite element modeling, which is in accord with the observed gradient but with a significant over prediction in the maximum strains. This is discussed in terms of stress relaxation during cooling or during storage by plastic deformation of the nodule, the matrix or of both. Relaxation by plastic deformation of the ferrite is demonstrated by the formation of low energy dislocations in a cell structure also quantified by the DAXM technique.

Key words: ductile cast iron, residual strain/stress, plastic deformation, differential aperture X-ray microscopy (DAXM)

1. Introduction:

Ductile cast iron (DCI) is an attractive engineering material, as it has strengths and toughness very similar to steel, and the machinability advantages make it very cost effective (Labrecque and Gagne, 1998). An example of industrial applications is the heavy components for wind turbine, e.g. the main shaft. One design requirement for such components is the good fatigue resistance, as the fatigue failure is a main failure mode during their design service life (Mirzaei Rafsanjani et al. 2014).

From a microscopic point of view, DCI is a composite material, consisting of graphite nodules embedded in a metal matrix which, in most engineering applications, can be either ferrite, or pearlite or a mixture of the two (Labrecque and Gagne, 1998). The differences in the thermal expansion coefficients between the metal matrix and the graphite nodules can lead to local thermal residual stresses in the composites during cooling from the processing temperature to room temperature (Ho and Lavernia, 1995; Withers and Bhadeshia, 2001). Due to the presence of the local residual elastic stresses, fatigue cracks may be initiated at the nodules because of overstain, as the local residual stresses may be larger than the flow stress of the metal matrix. But they may also be lower as they may relax by plastic deformation of the nodules or the surrounding volume (Barlow and Hansen, 1991). In the past many studies have been conducted to quantify and model the residual stresses in metal matrix composites containing particles that are harder than the metal matrix, e.g. SiC or Al_2O_3 reinforced aluminum matrix composite (Arsenault and Taya, 1987; Ledbetter and Austin, 1987) and Al/W metal matrix composite (Poulsen et al., 1997). For a system like DCI, where the particles (graphite nodules) are considerably softer than the metal matrix, there has however not been much knowledge about the local residual stress. Many researchers believed the local residual stresses to be minor, considering the fact that graphite is soft; and the local residual stresses were neglected in most micromechanical models (Hütter et al., 2015). However, recently the formation of residual stress comparable to the material yield stress has been predicted by finite element models in DCI (Andriollo et al., 2016). To optimize design and processing of DCI components, the magnitude of the local residual stresses must therefore be known.

It is however a challenging task to quantify local residual stresses experimentally. Recently, the development of new experimental characterization techniques has given promising possibilities. For example, a novel synchrotron X-ray technique, the so-called differential aperture X-ray microscopy (DAXM), has been developed during the last 15-20 years for non-destructive 3D characterization of microstrucrure and local elastic strains (Larson et al., 2002; Levine et al., 2006). With DAXM, local elastic strain distribution inside individual grains has been measured in e.g. deformed bicrystal Ni (Ohashi et al., 2009) and NiAl-Cr(Mo) composite (Barabash et al., 2012). The use of focused microbeam offers spatial resolutions of sub-micrometers (Ice and Pang, 2009).

In this study, we use DAXM to characterize the microstructures and local residual strains/stresses in only matrix grains at graphite nodules in a DCI. No microstructures and strains are obtained from the graphite nodules, as the diffraction signals from them are weak. The objective of the study is to answer the following questions: i) are the matrix grains plastically deformed? ii) what is the magnitude of the residual elastic stress and is it comparable with the flow stresses of the cast iron? iii) how the residual elastic stress distributes? and iv) how residual stress relaxes? A DCI is chosen based on a previous study, where the fatigue properties of the DCI are already available in a large data base. The results on the local residual stresses will provide a new aspect to evaluate the obtained fatigue properties.

2. Experimental

2.1 Samples

A metal mold ductile cast iron was extracted from the head of a sample that has been fatigue tested to fail after ~5 million cycles under stress level 5 as described in (Mukherjee et al. 2016). The sample consists of almost spherical graphite nodules and a metal matrix with a relatively homogeneous structure, being mainly ferrite with a small fraction of perlite (~5%). The graphite nodules were distributed relatively homogenously in the metal matrix (see Fig. 1a). The mean size (equivalent circle diameter, ECD) and volume fraction of the graphite nodules were ~30 µm and 11.5%, respectively. The mean distance between nodules and the maximum nodule size are both ~70 µm. The ferrite matrix has an average grain size of ~30 µm (Fig. lb), measured by electron backscattered diffraction in a Zeiss Supra 35 scanning electron microscope using a Channel 5 software from HKL Technology. The chemical composition of the sample is listed in table 1.

Table 1. Chemical composition of the sample (mass%).

C	Si	Mn	P	S	Cr	Ni	Co	Cu	Ti	V	Mg	Ce	Se
3.68	2.30	0.22	0.015	0.011	0.027	0.048	0.024	0.016	0.017	0.014	0.11	0.042	0.043

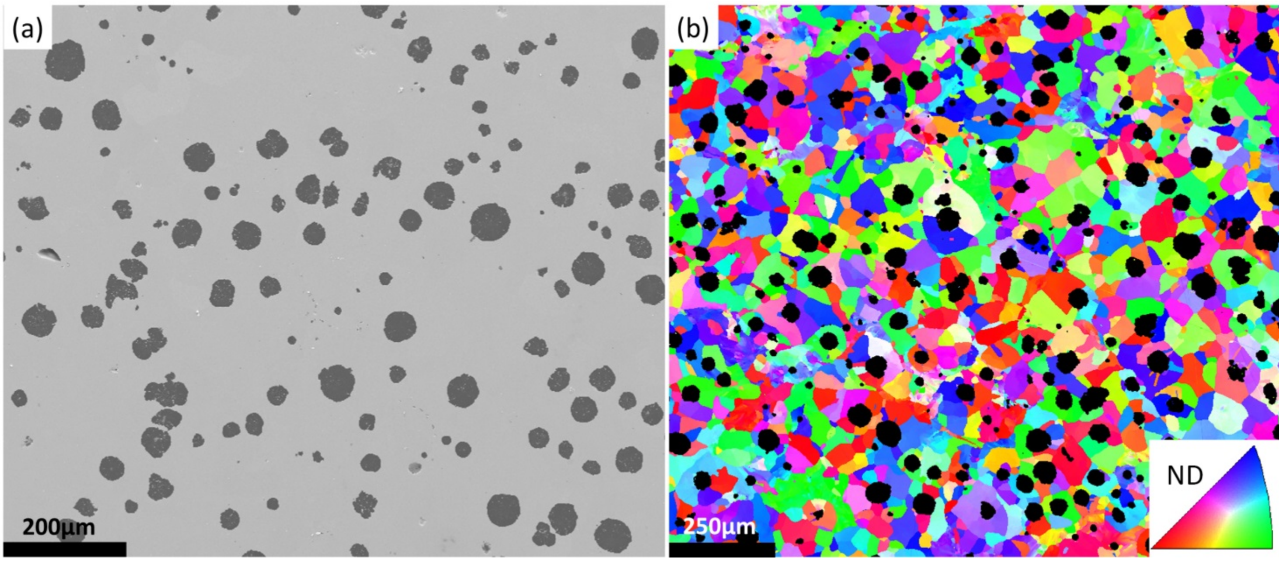

Fig. 1 Microstructures of the DCI showing the graphite nodules and metal matrix. (a) Scanning electron microcopy image and (b) EBSD map. In (a) dark regions are graphite nodules and the rest is metal matrix, while in (b) the black particles are graphite nodules and the colored grains are metal matrix. The colors of the matrix grains correspond to the crystallographic orientation along the sample normal direction (ND) (see the insert).

2.2. Lattice parameter

It is known that the ferrite lattice parameter depends on the amount of solute elements (Bhadeshia et al., 1991). For the present material, the main alloying elements, i.e. C, Si, and Mn, were considered for the calculation of the lattice parameter. The resulting ferrite lattice parameter was calculated using a function that was deduced based on various publications (Bhadeshia et al., 1991):

$$a_0 = a_{Fe} + (3a_{Fe}^2)^{-1} \times [(a_{Fe} - 0.001297w_C)^2(a_{Fe} + 0.011606w_C) - a_{Fe}^3] - 0.0006w_{Si} + 0.0006w_{Mn} \qquad (1)$$

where $a_{Fe} = 2.8664$ Å was the lattice parameter of pure ferrite, and w_x is the weight percentage of x element (x = C, Si and Mn). For the present sample, the Si and Mn contents listed in table 1 were used for determining the lattice parameter, while a maximum solubility of 0.005% at room temperature for the C content was used in the matrix grains. The lattice parameter for the current ferrite was then calculated to be a_0=2.8653 Å using Eq. 1.

2.3 X-ray tomography

To assist synchrotron measurements, the 3D distribution of the graphite nodules was characterized by X-ray tomography using a Zeiss Xradia 520 Versa micro-CT system. For the CT scan, a polychromatic conical beam with X-ray energies up to 140 keV and 1401 image projections over a rotation of 360° were used. For the present study, two nodules with size ≥50 µm were selected for residual stress measurements: one nodule beneath the sample surface, defined as nodule A, and one nodule exposed to the sample surface, defined as nodule B, see Fig. 2. Nodule A represents a bulk nodule, while nodule B represents a surface nodule. Part of another nodule, which was neighboring to nodules B, has coincidently been illuminated. Some of the result around this nodule is also included in the analysis, and this nodule is defined as nodule C. The distance of center-of-mass between nodule B and C is about 95 µm. Nodule A is about 400 µm away from nodule B/C. The sizes and distances between the center-of-mass of the selected nodules and the sample surface are given in Table 2.

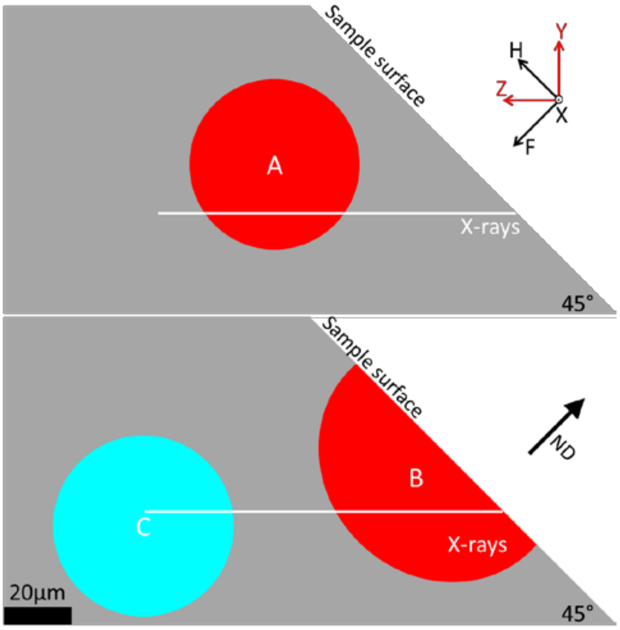

Fig. 2. Sketches showing a side view of the detailed scanning position relative to the selected nodules. The selected nodules are marked by A, B and C. Sample normal direction (ND) is marked by the black arrow. The white lines represent the mapping planes illuminated by the incoming X-rays, which are along the Z direction.

Table 2. Sizes and positions of the selected three nodules.

GN no.	Diameter (µm)	Depth (µm)[a]
A	50	40
B	72	10
C	63	78

[a] Depth means the perpendicular distance from the center-of-mass of the nodules to the sample surface.

2.4 DAXM experiment

The differential aperture X-ray microscopy (DAXM) was performed at beam line 34-ID-E at the Advanced Photon Source (APS), Argonne National Laboratory, USA (Liu et al., 2010). In the DAXM experiment, the X-rays were focused at the sample using two non-dispersive Kirkpatrick-Baez (K-B) focusing mirrors. The resulting microbeam has a Lorentzian profile and a full-width half maximum of ~0.5 µm. The sample was mounted on an inclined sample holder at a 45° incidence angle to the incoming X-ray beam, and was scanned horizontally by moving the sample stage with a step size of 1 µm. Two sections through the selected nodules were scanned. The detailed scanning position relative to the selected nodules is sketched in Fig. 2b. The Laue diffraction patterns from the whole volume within the incident microbeam were recorded on a flat panel detector (409.6×409.6 mm^2, 2048×2048 pixels) mounted in 90° reflection geometry 510.3 mm above the sample. The detector's geometry with respect to the incident beam was calibrated using a standard strain-free silicon single crystal. To resolve the diffraction pattern from each volume element at different depths, a Pt-wire of 50 µm diameter was used as a differential aperture and scanned at a distance of ~100 µm from the sample surface. The Laue patterns at each depth were reconstructed by ray-tracing algorithm using the LaueGo software available at APS beamline 34-ID-E (Tishchler, 2014). The reconstructions were conducted to a depth of about 100 µm into the sample with a step size of 1 µm.

Two beam modes were used in the present study: first a polychromatic beam was used to determine the orientations and deviatoric strains of the matrix grains; then a monochromatic beam was used for determining absolute lattice parameters of selected grains in the mapped sections. Two examples of depth-resolved Laue diffraction patterns from polychromatic scans are shown in Fig. 3a and 3b. The patterns were indexed using also LaueGo software, from which the hkl indices of individual spots as well as their corresponding X-ray energies were determined as byproducts of the orientation and strain analysis (Tishchler, 2014). Based on the energies and spot positions, one crystallographic plane with normal approximately parallel to the sample normal direction, was chosen for the monochromatic energy scan for each selected grain. From this energy scan, the intensity distributions as a function of the diffraction vector, $Q = 2\pi/d$ (Q-distribution) were determined for the selected diffraction spot at all depths, see for example Fig. 3c, which was obtained from the Laue spot (-3 2 5) in Fig. 3a. At each depth, the Q-distribution was fitted using a Gaussian function and the center of the distribution, Q_C, was used to determine the absolute diffraction plane spacing, d (see Fig. 3d).

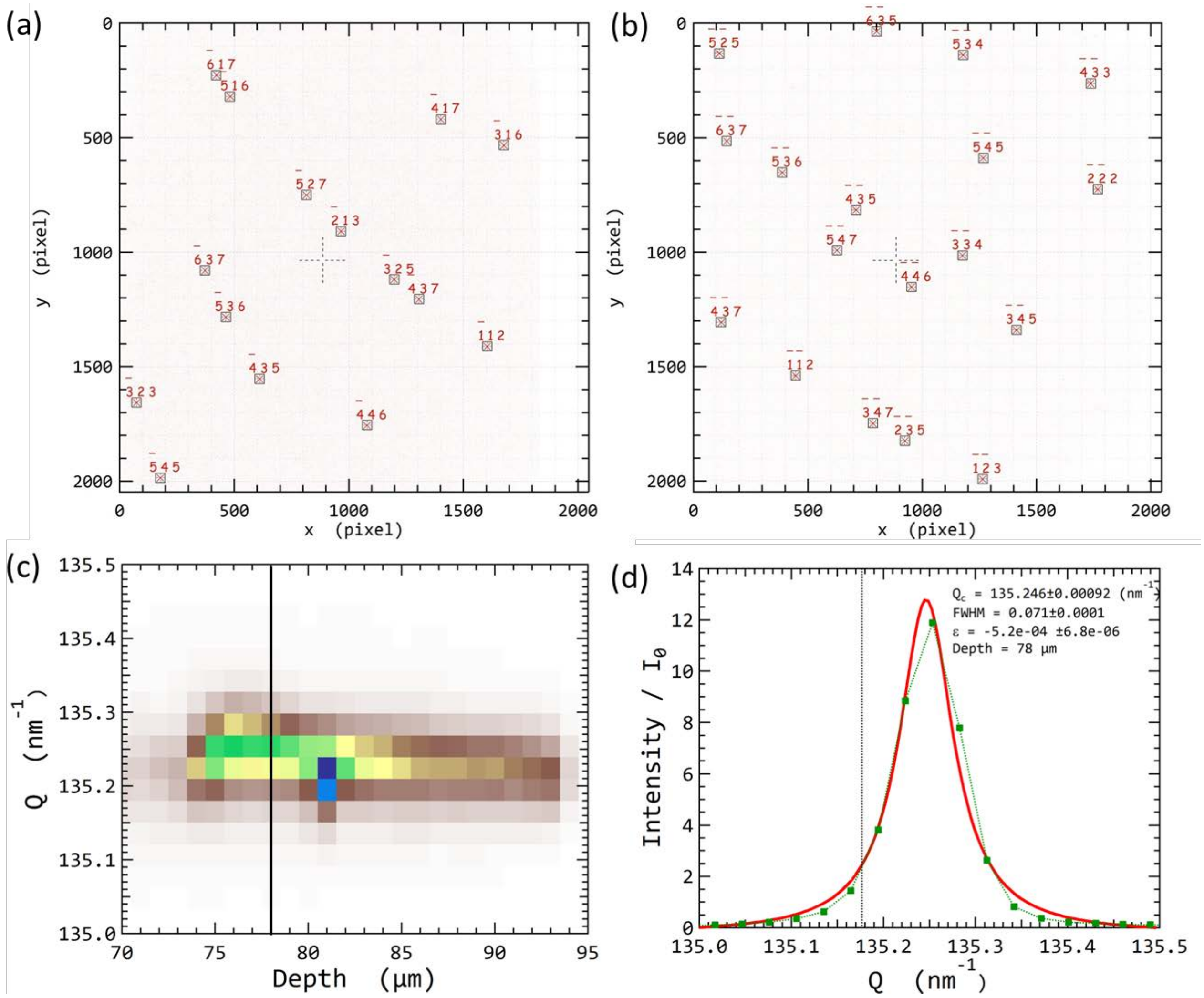

Fig. 3 Illustration of orientation indexing based on white beam Laue diffraction patterns and determination of crystallographic plane spacing. (a) and (b) show two examples of indexed depth-resolved Laue diffraction patterns. (a) and (b) are from the grains marked by white boxes in Figs. 4a and 4b, respectively. The crosses in dashed lines in (a) and (b) mark the diffraction center. (c) The diffraction vector, Q, as a function of depth for one wire energy scan corresponding to the (-3 2 5) Laue spot in (a). (d) Fitted intensity distribution for the (-3 2 5) Laue spot for the depth marked by black vertical line at the frame in (c). The center of the fitted Q-distribution, Q_C, is used for determination of the crystallographic plane spacing. The dashed line in (d) marks the Q value for d_0 of the (-3 2 5) crystallographic plane determined based on the lattice parameter in section 2.2.

3. Results

3.1. Depth-dependent grain orientation distribution from polychromatic scans

The depth-dependent 3D grain orientation distributions obtained from DAXM around the selected nodules are shown in Fig. 4. Here the ferrite matrix around the selected nodules is shown in color and the graphite nodules are shown as black sphere-like blocks. The three selected nodules are marked by A, B and C. Two neighboring graphite nodules are also partly seen. In the matrix grains, a critical angle of ~0.1° is used for revealing the detailed boundary structure, and a critical angle of 3° is used for defining grains in the matrix. It is evident that most of the grains are deformed containing dislocation boundaries with misorientation angles below 1°, and the dislocation boundaries are organized in a cell structure. Only a few grains with relatively small sizes (<25 μm) are nearly deformation-free (see the numbered grains in Fig. 4). This may be related to an effect of grain orientations (Huang and Winther, 2007).

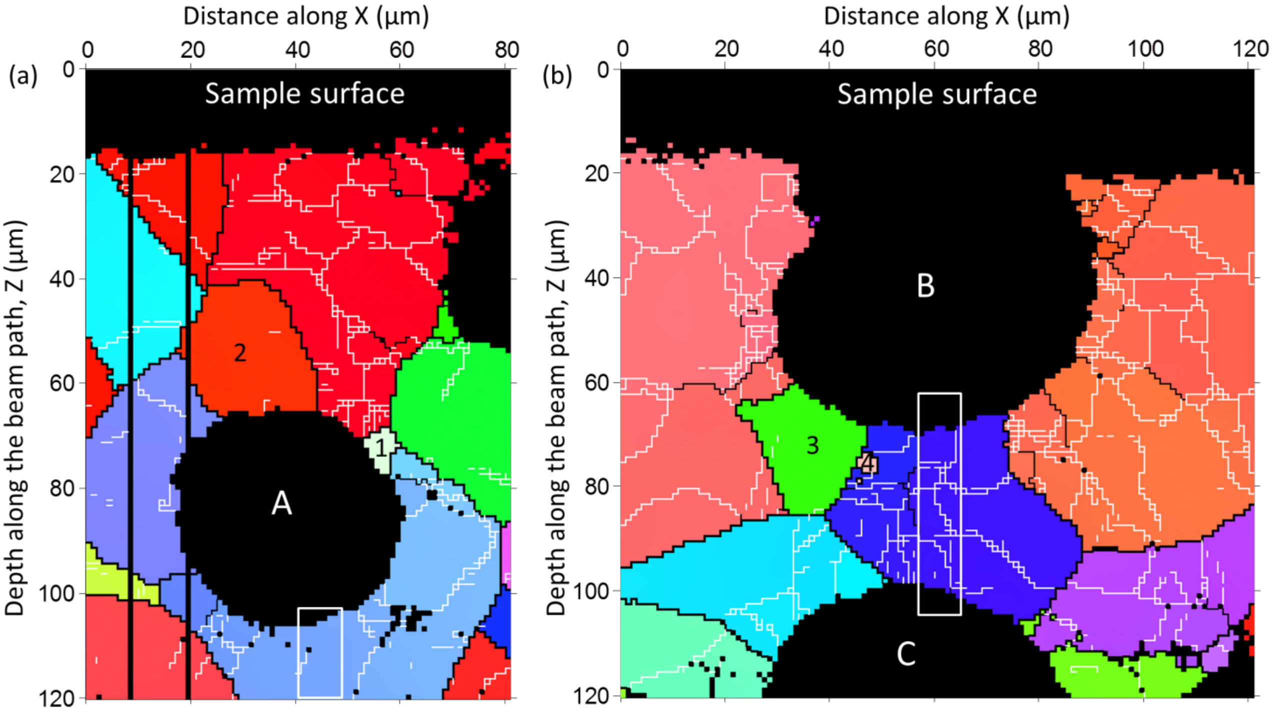

Fig. 4 Microstructures of the DCI near selected nodules characterized using white beam DAXM. (a) and (b) showing microstructures around the selected graphite nodules A and B/C, respectively. In the maps, dislocation boundaries with misorientation angles in the range of 0.1 – 1°, 1 – 3°, and > 3° are shown in thin black, thick white and thick black lines, respectively. The colors of the matrix grains correspond to the crystallographic orientation along the sample normal direction in the sample coordinate system (XHF system in Fig. 2). The color code is the same as that in the insert in Fig. 1b. The two white boxes mark regions where monochromatic energy scans were conducted. The numbers mark grains, which are nearly deformation-free. The two black lines in (a) were caused by a technical fault during the Pt-wire scans, and the data were not recorded for that two positions. The black individual pixels in the matrix away from the nodules are non-indexed.

The grains around nodule B contain evidently more dislocation boundaries as well as more boundaries with misorientation between 1-3° (seen as thick white lines) than those around nodules A and C. To quantify the local plastic strains around the nodules, the average dislocation densities within the grains around the nodules and at different distances from the nodule/matrix interface are calculated based on the microstructures. All dislocation boundaries with misorientation angles in the range 0.1-3° are included for the calculation, i.e. the grain boundaries are not included (Hansen, 1994). The results are shown in Fig. 5. It is found that the average dislocation densities are large at places close to the nodules, and decrease with increasing distance from the nodule/matrix interface. The maximum dislocation density around nodule B is

~6.4 × 10^{12} m^{-2}, which is about twice of those around nodules A and C. The dislocation density in the matrix away (>20 µm) from nodule is in the range 1.2-1.6 × 10^{12} m^{-2}.

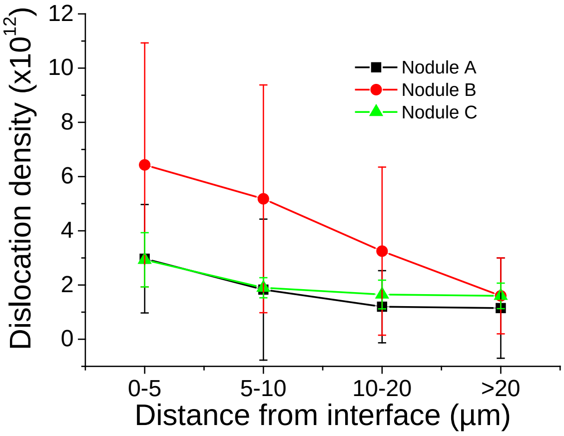

Fig. 5. Average dislocation density as a function of distance from interface. The dislocation densities are calculated from the dislocation boundaries with misorientation angles in the range 0.1-3° (Hansen, 1994). The error bars were estimated based on the variations in the distances between the dislocation boundaries, reflecting the differences between matrix grains.

3.2. Monochromatic energy scans

Two grains marked by white boxes in Fig. 4 were chosen for the monochromatic energy scans to determine the absolute crystallographic lattice plane spacings. Diffraction from the (-3 2 5) and (-3 -3 4) planes were used for the grains around nodules A and B/C, respectively, as their normals are nearly parallel to the sample normal direction (see Fig. 3a and b), with deviation angles of ~7° and ~6°, respectively. Based on the measured absolute crystallographic plane spacings and the lattice parameter specified in section 2, the strains along the selected crystallographic directions (roughly perpendicular to the nodule/matrix interface) were determined. For the areas around nodules A and B/C, a line step size of 1 µm and 2 µm, respectively, was used.

The results are shown in Fig. 6. For the grain around nodule A, compressive strains are observed for most part of the grains, and they are higher at regions close to the interface than at the interior volume. For the grain in-between nodules B and C, compressive strains are observed at regions close to the nodule/matrix interface, while nearly zero strains are seen in the middle of the characterized area of the grain. The compressive strains at the interface around nodule C are generally larger than those around nodule B. The maximal compressive strain is -8 × 10^{-4} and -6.3 × 10^{-4} for the grains around nodule A and B/C, respectively. It should be noted that the maximal compressive strain is found at the interface for nodule C but about 2-5 µm away from the interface for nodule A. Within the grains, strain change rather smoothly, and no abrupt change is seen at the dislocation boundaries (see the microstructure within the white boxes in Fig. 4).

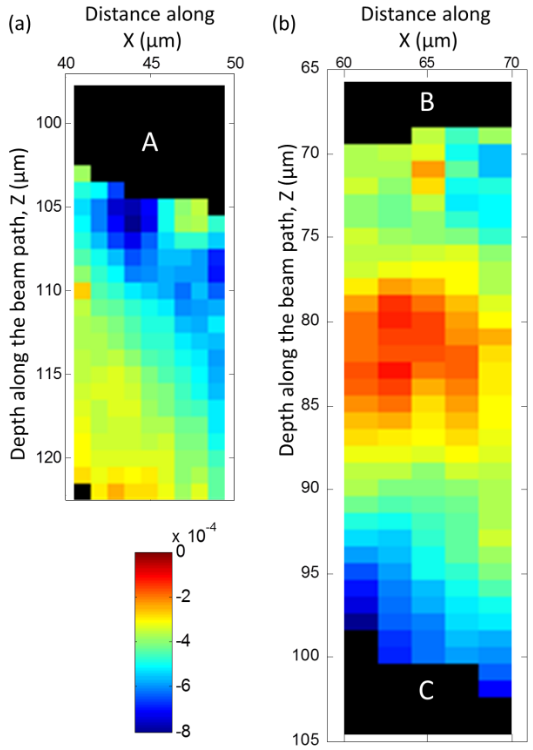

Fig. 6 Maps colored according to the strains determined based on the monochromatic energy scans. The strains in (a) and (b) are calculated along the [-3 2 5] and [-3 -3 4] directions for the grains marked by the white boxes in Fig. 4a and 4b, respectively.

3.3 Deviatoric strains

The deviatoric strain components, which represent the lattice shape changes, at each depth were determined automatically (Chung and Ice, 1999) using the LaueGo software. The strain component maps of the matrix grains around nodule A are shown in Fig. 7, where the grain boundaries and dislocation boundaries shown in Fig. 4 are superimposed to the strain component maps. The strains were determined in the sample coordinate system (i.e. XHF system in Fig. 2). It is evident that most of the extreme values of the calculated strains are related to dislocation boundaries. Some boundaries affect only one pixel (1 μm) distance from the boundaries, while others affect 4-5 pixels distances. As discussed in Refs. (Barabash et al., 2003; Larson and Levine, 2013), these values are not reliable as the determination of deviatoric strains are sensitive to the dislocation boundaries, which result in streaking in the Laue diffraction patterns and in turn exaggerate severely the deviatoric strains. Beside those extreme cases, the majority of the strain components is in the range -1.2 — 1.2 $\times 10^{-3}$. Large local strain variations are seen in all the strain component maps. These variations are both between different grains and within individual grains and cells. The differences between grains may due to the differences in crystallographic orientations. The shear strain components in the sample normal plane (ε_{13} and ε_{23}) appear noisier than the other strain components. This is mainly because that these shear strain components are relatively sensitive to the origin of the diffraction (Lynch et al., 2014; Poshadel et al., 2012). There is no apparent difference in strain variations between the grains around the nodule and those away from the nodule.

When inspecting grains along the nodule circumferential direction, the ε_{33} strains change gradually from mainly compressive at the bottom side of nodule A to mainly tensile at the top side of nodule A. The opposite is seen for ε_{11}. Mainly compressive strains are seen for ε_{22}. For ε_{23} mainly tensile strains are seen at the top and bottom sides, while mainly compressive strains are at the left and right sides of nodule A. For ε_{12} and ε_{13} the change in strain along the circumferential direction is more complicated. Along the nodule radial directions, strain gradient is seen within some of the grains/subgrains around nodule A, for example within the area marked by white box in Fig. 4a. Fig. 9a shows a magnified and rescaled ε_{33} map for this grain. A strain gradient very similar to that observed in Fig. 6a is seen, though a slightly larger gradient for deviatoric strain ε_{33} is seen.

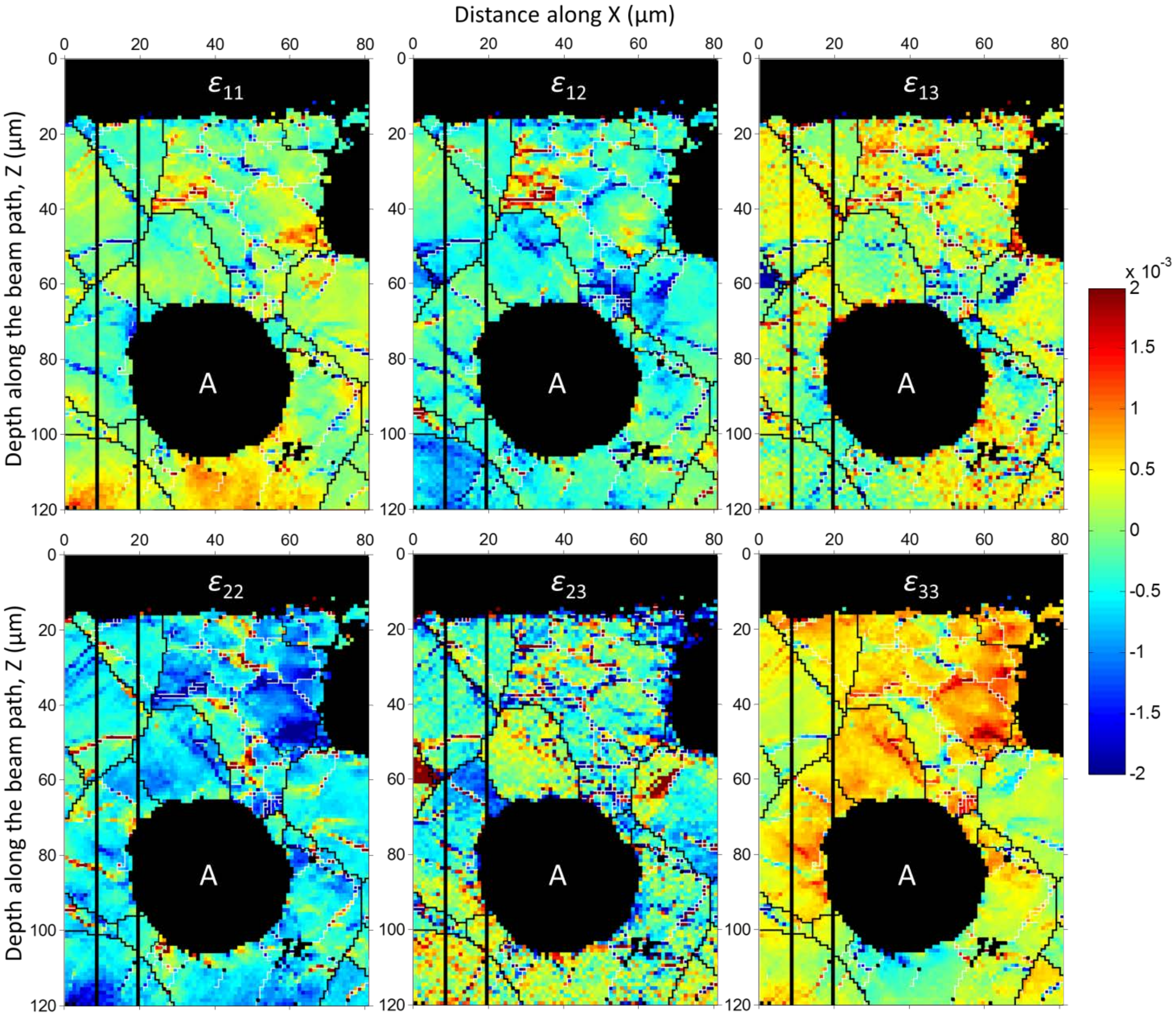

Fig. 7 Deviatoric strain maps colored according to the deviatoric strain components for the microstructure around nodule A.

The areas with non-reliable extreme strain values are larger around nodule B than around nodule A (see Fig. 8). This is mainly due to the fact that there are more dislocation boundaries (also with relatively high misorientation angles) in the matrix grains around nodule B than around nodule A. The patterns of strain changes along the circumferential direction of nodule B are about similar to those around nodule A, although the top part of nodule B is at the surface and thus missing in the scans. The local strain gradient along the radial direction of nodule B is however difficult to be examined in most of the grains, as those grains contain dislocation boundaries, which results in non-reliable deviatoric strain values. An example is shown in Fig. 9b, where the ε_{33} map for the area marked by the white box in Fig. 4b is enlarged and rescaled. The strain gradient observed from the energy scan in Fig. 6b is not seen in Fig. 9b. As only grains around part of the nodule C are seen, the strain changes along the circumferential direction cannot be examined. The local strain gradient along the radial direction of nodule C is seen for some grains, but becomes complex for the grains close to the top part of nodule C. This is likely to be due to interaction effects from the neighboring nodule B.

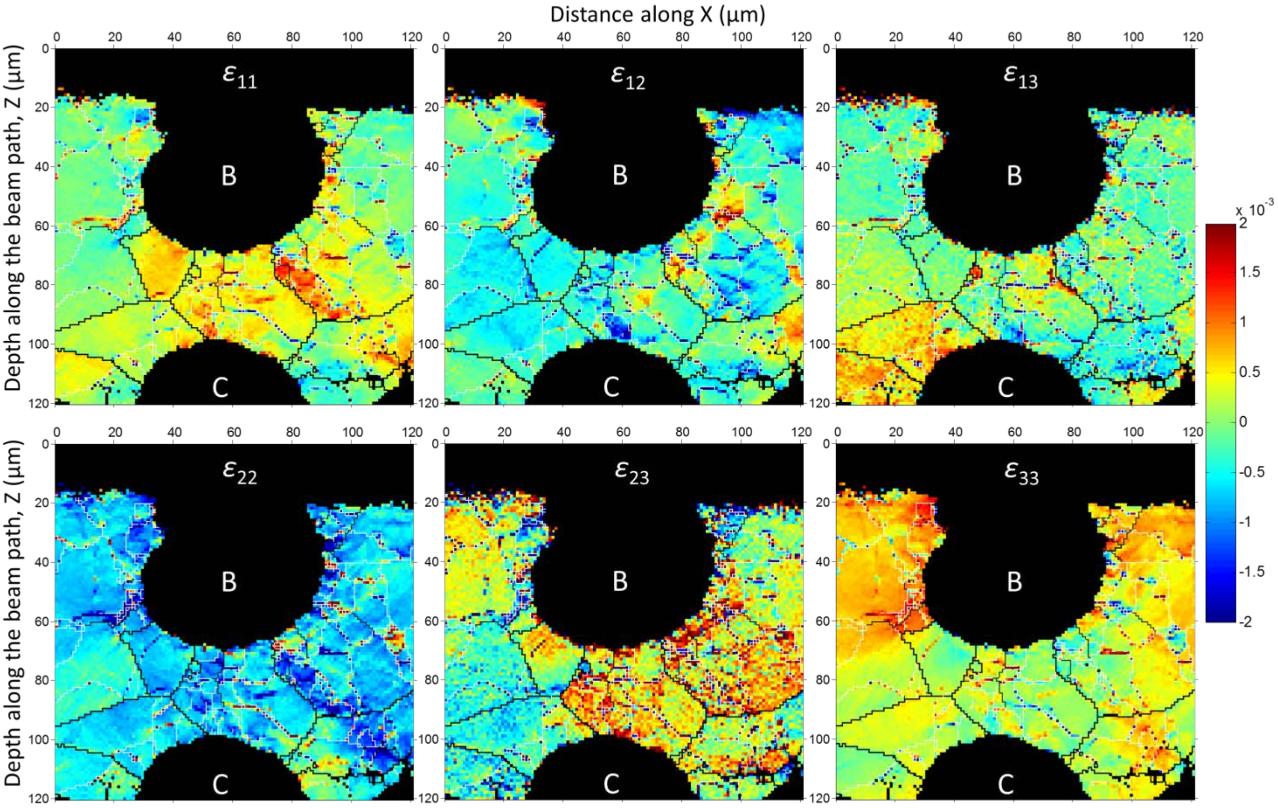

Fig. 8 Deviatoric strain maps colored based on the deviatoric strain components for the microstructure around nodule B/C.

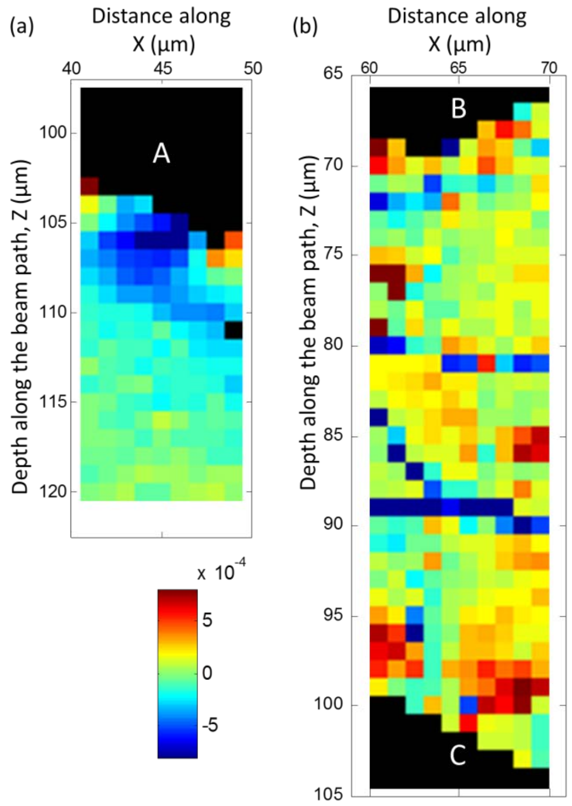

Fig. 9 Strain map colored according to the deviatoric strain component ε_{33}. The strains in (a) and (b) are for the grains marked by the white boxes in Fig. 4a and 4b, respectively.

4. Discussion

The present study demonstrates that DAXM is a powerful and unique technique for non-destructive 3D characterization of both microstructure and local residual strain for the ferrite matrix grains within a 3D volume in the present DCI. By using focused microbeam with size of 0.5×0.5 μm^2, a spatial resolution of 1 μm in depth is obtained. With the polychromatic beam mode of DAXM, the local dislocation cell structures around the nodules are revealed with an angular resolution of ~0.1°. With the monochromatic energy scan of DAXM, the local elastic strains are measured for the two selected grains with a resolution of 1×10^{-4}. To the best knowledge of authors, no other techniques can provide such good combination of depth-dependent spatial, angular and strain resolutions within local volume of 1 μm^3. From the Laue patterns, the deviatoric strains are also determined, although only the deviatoric strains determined within those relatively large grains/subgrains that contain less dislocations or dislocation boundaries with very low misorientation angles (about 0.1°) are reliable (Larson and Levine, 2013) (e.g. the deviatoric strains in Fig. 9a).

With these techniques, the results have shown evidently that ferrite matrix grains at the nodules are plastically deformed, most at large nodules. Differences in plastic strains and elastic strains are seen between different grains around the nodules, which may be due to the effects of crystallographic orientations, causing differences in slip pattern. Both plastic and elastic strain gradients are seen in the matrix grains at the nodules. In the following, the existence of the residual elastic strain gradients and their formation mechanism will be discussed. For the latter, a finite element modeling that was developed in a previous publication (Andriollo et al., 2016) is used to calculate the residual strains. The last three questions raised in the Introduction will be addresses based on the discussion. In addition, the effects of nodule sizes as well as surface on the residual strains/stresses, and their roles in the material fatigue properties are discussed in the end.

4.1 Residual elastic strain gradients in the matrix grains around nodules

The measured elastic strains depend on the lattice parameter, which according to Eq. (1) varies with variations in local chemical contents. The present monochromatic energy scan shows that there are significant compressive strains along the sample normal direction with maximum of 6.5-8 × 10^{-4} and a gradient of 5-6 × 10^{-4} over a distance of ~20 µm around the nodules (see Fig. 6). Although the strain resolution is 1 × 10^{-4}, one may speculate that the measured strain gradients are just a reflection of gradients of chemical contents in the matrix. This speculation is not inurbane, as it is well known that during solidification process of DCI, certain alloys' elements segregate, including the main alloy elements C, Si and Mn in the present DCI (Alhussein et al., 2014). This possibility can however be ruled out by following analysis.

During solidification Si is generally segregated at the first solidification region around graphite nodules, leading to a high Si content there, and a low Si content at the last solidification region, i.e. at the joints of eutectic cells. Mn segregates in a reverse way, i.e. low Mn content close to the nodules and high content within the eutectic zones (Alhussein et al., 2014). Our measurements were conducted within matrix grains that contact directly the graphite nodule (nodule A), or within a matrix grain directly in contact to two nodules (B and C). Therefore it is very likely that the characterized region is within the first solidification region, especially for the grain between nodules B and C. The Si/Mn contents there should be higher/lower than the average Si/Mn contents in the material. If we assume that the Si/Mn contents were ~20% higher/lower within the characterized region than the average percentage of the sample, i.e. 2.76% and 0.18% for Si and Mn, respectively, the measured compressive strain will reduce only about 1 × 10^{-4}, which is much smaller than the observed strain. But it has to be noted that the chemical difference considered here is between the first solidification region and the last solidification regions. The chemical variation within the first solidification region should be even less than that (Dong et al., 1997; Vazehrad et al., 2015). According to Eq. (1), a strain difference of 5-6 × 10^{-4} requires Si + Mn variation of 2.5-3%, which is almost more than the total average chemical contents of Si + Mn in the material. It is therefore almost impossible that so large chemical variations can exist within the two characterized matrix grains.

Additionally, C is another main element in DCI that can affect the lattice parameter. In the present paper, we assumed the C content to be the maximum solubility of (0.005%) of C in ferrite at room temperature. From Eq. 1, it can be seen that in order to reduce the lattice parameter, and thus reduce the observed compressive strain, the C content should be even less. However, in total the 0.005% C changes only the strain about 5 × 10^{-5}.

Last but not least, a similar magnitude of compressive strains and a slightly larger strain gradient are also seen in the deviatoric ε_{33} map for the marked grain around nodule A (see Fig. 9a). As the refinement of the deviatoric strains does not depend on the input lattice parameter, the measured strain gradient therefore must be real. Based on this evidence and the analysis of chemical contents, it can be concluded that the observed compressive strains and strain gradient over the 20 µm distance from the interface is not simply due to chemical variations but a real existence. To further analyze the formation of the local residual strains, a computer model using finite element method is conducted and described in the following section.

4.2 Finite element modeling

Several analytical models (Ho and Lavernia, 1995) are available in the literature to predict the formation of thermal residual stresses in materials containing secondary-phase particles, where Eshelby's equivalent inclusion method (Eshelby, 1957) is central, assuming homogeneity of the material constituents at the micro-scale. In ductile iron, however, this assumption does not hold, due to the heterogeneous and anisotropic nature of the graphite nodules (Theuwissen et al., 2014). To overcome this limitation, Andriollo et al have recently proposed a new finite element model where the nodules' internal structure is explicitly taken into account (Andriollo et al., 2016). This model was applied to the present ductile iron assuming a graphite volume fraction of 11.5 % and 48 conical partitions in the nodule. Time-independent plastic deformation in the matrix, neglected in the original version of the model, was here simulated via a standard J2-flow formulation, considering two different sets of properties: strain-stress curve at room temperature (Zhang et al., 1999), and temperature-dependent flow stress (Bonora and Ruggiero, 2005).

The patterns of the predicted residual elastic strains in the matrix around the graphite nodule are complex, having a cubic symmetry and with each strain component varying along both the circumferential and radial directions. For the comparison to the experimental data, only the predicted ε_{33} component (in the XHF system) along a path which is equivalent to the left vertical line of the white box in Fig. 4a is considered. Comparison with the results based on the monochromatic energy scans around nodule A (Fig. 6a) is reported in Fig. 10, where the measured strains are plotted as line profiles, with each curve representing one vertical line in Fig. 6a. It can be seen that the general tendency of the measured compressive strains to decrease with increasing distance from the interface is captured by the finite element model. However, the maximum compressive strain close to the nodule and the corresponding decreasing rate are over-predicted by a factor ~2.

There could be several possible reasons that the maximum compressive strains from experiments are smaller than those predicted by modeling. Firstly, some plastic deformation in the matrix grains is seen for the selected nodules (see Figs. 4 and 5). The plastic strain estimated based on the dislocation densities is maximum about 2×10^{-4} (Hansen, 1994), which is similar to the plastic strain predicted by the model (Fig. 10), but relatively small compared to the differences between the measured and modeled strains. At the same time, when a material is plastically deformed and kept at a constant strain, stress relaxation occurs (Dotsenko, 1979). This mechanism can contribute also to the observed reduction in the measured residual strains. Secondly, it is assumed in the model that no plastic deformation occurs in the nodule. In reality, this assumption may not be hold. Moreover, high-temperature creep could also reduce the elastic strain. And in the model, an isotropic matrix is used, while in reality the anisotropy of the single ferrite grains may also induce some strain variations (see Figs. 7 and 8).

Another inconsistency between the model and experimental results is that the peak positions of measured maximum residual strains along each line are not as model predicted at the interface, but at a distance of 2-5 μm away from the interface. The compressive strains drop about $5 \times 10^{-5} - 3 \times 10^{-4}$ in this range for all lines. This strain drop is however not observed at nodule C (see Fig. 11c), i.e. it is not a typical phenomenon. It could be due to some local microstructural variations in 3D that have not been capture by the present characterizations. To clarify this point, further characterization will be performed in the future.

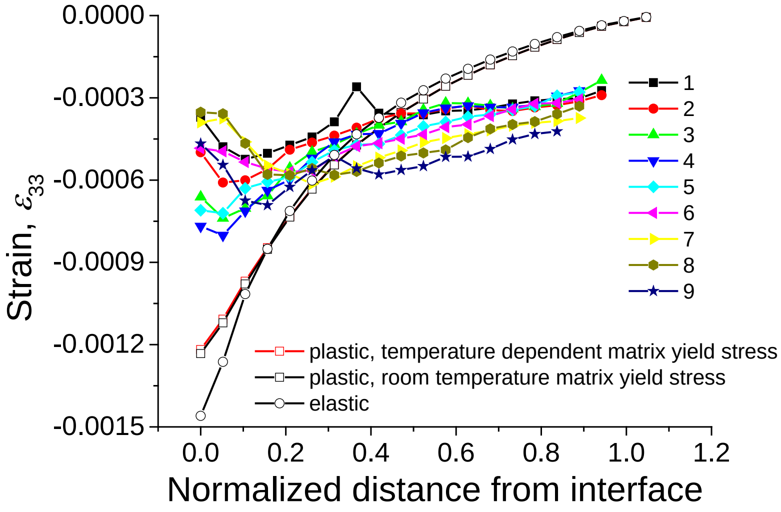

Fig. 10 Comparison between the experimental and modelling strain line profiles. The line profiles for the experimental curves are converted from the data shown in Fig. 6a, each curve corresponds to each vertical line, numbered from left to right. The experimental curves are calculated along a path which is equivalent to the left vertical line in Fig. 6a.

4.3. Size and surface effects on the residual stresses

By combining the DAXM with the X-ray µ-CT, it is possible to evaluate the effect of the nodule size on the residual stresses. To make comparison between nodules, the residual stresses were approximately derived from the measured residual strains by means of the directional Young's moduli. The directional Young's moduli along the two crystal directions, [-3 2 5] and [-3 -3 4], are calculated to be 220 and 270 GPa, respectively, using the elastic constants for pure iron from Ref. (Hashin and Shtrikman, 1962).

The calculated stresses as a function of distance from interface along vertical lines are shown in Fig. 11. A similar maximum compressive stresses are seen for the grains around nodules A and C, while relatively small compressive stresses are seen for the grain around the nodule B. The 3D sizes of the nodules A and C are similar (see Table 2). It is thus reasonable that the compressive stresses around nodule A and C are similar. The size of nodule B is bigger than the other two nodules. It is therefore interesting that the compressive stresses over the whole range are smaller than those within the grain/subgrain around nodule A and C.

Two major possibilities should be considered. Firstly, as shown in Fig. 5, the dislocation density in the matrix grains around nodule B is higher than those around nodule A. The residual stresses are relaxed more by plastic deformation in the matrix grain around nodule B than those around nodule A. On the other hand, the higher dislocation density also implies that higher stresses existed during cooling. It is however difficult to quantify these two effects based on the present experiment. Secondly, the nodule B is exposed at the sample surface. The residual stresses at the interface around B are compressive stresses along the sample normal direction. When the nodule B was completely inside the bulk material (i.e. before polishing), the compressive stresses at one side of the interface were counterbalanced by the compressive stresses at the opposite side, and the local compressive stresses can be maintained. However, when the nodule B is exposed to free surface, the compressive stresses opposite to the side we measured were released. The compressive stresses at the inner interface are then pushing the nodule out of the surface, and are consequently reduced. The free surface releases not just the stresses at the interface. The stresses at the volume in the middle of the characterized grain between nodule B and C (~15-20 μm from the two interfaces) seem also to be affected, for a relatively small magnitude of compressive stresses are seen at that position compared to those at the volume away from nodule A (>15 μm from the interface).

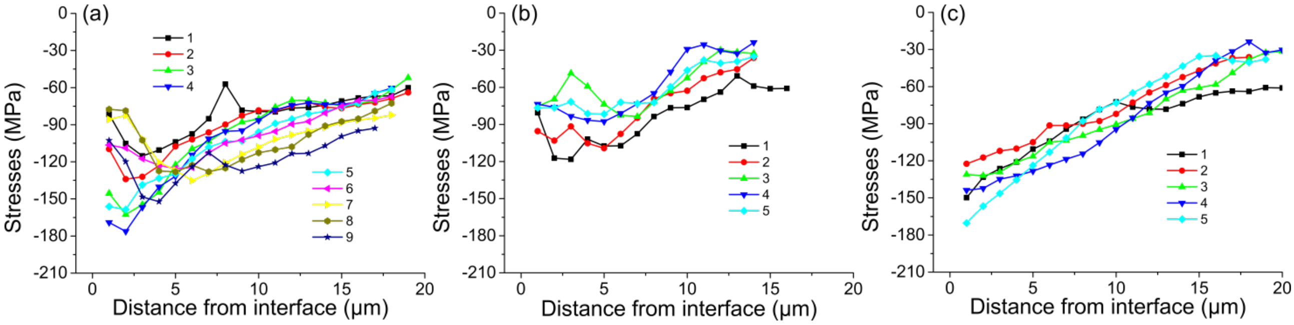

Fig. 11 Residual stresses calculated based on the measured strains from the monochromatic energy scans as a function of distance from interface for nodules. (a) - (c) are for the strains measured in the matrix grains near nodules A - C. The line profiles are calculated based on the strain data shown in Fig. 6, each curve corresponds to each vertical line, numbered from left to right.

Large nodules are selected for the present study, as they are the critical ones for the fatigue tests (Verdu et al., 2008). The maximum residual stress at the selected nodules is about half of the yield stress of the matrix, which is about 297 MPa (Bonora and Ruggiero, 2005). The residual stresses in the matrix grains can therefore not be neglected for the material fatigue properties. The maximum strength calculated based on dislocation densities (Hansen, 1994) in the matrix grains is about 35 MPa for the largest nodule. Altogether, the residual stresses are still not so critical for the fatigue properties of the present DCI, and that might be a reason for the high fatigue cycles for this DCI (Mirzaei Rafsanjani et al. 2014). For other DCI, where the largest nodule size can be >200 μm (Mukherjee et al. 2016), the resulting residual stresses may be critical for the fatigue life. However, the large nodule size forms typically due to slow cooling rates, which at the other hand can reduce the residual stresses. How these two factors are balanced needs to be analyzed. At the same time, other factors as the nodule connectivity and shape as suggested in the previous study may also be critical for the material fatigue properties (Mukherjee et al. 2016). The effects of these factors on the residual stresses (thus on the fatigue properties) are planned to be examined in the experiments at APS.

5. Conclusions

1. The DAXM technique is suitable for characterization of both local plastic and elastic residual strains in the present ductile cast iron. With these techniques, an angular resolution of 0.1°, a spatial resolution of 1 μm, and an elastic strain resolution of 1×10^{-4} have been obtained. Additionally, reliable deviatoric strains are obtained based on the depth-resolved polychromatic Laue patterns for the grains/subgrains that contain no or little dislocations/dislocation boundaries.

2. The ferrite matrix grains at nodules have been plastically deformed as a result of the local stresses developed due to the interaction between the nodules and the matrix during cooling. The plastic deformation is observed in the form of dislocation boundaries with low misorientations angle in the range 0.1-1°, and organized in cell structures, and most pronounced near the large nodule.
3. Compressive residual elastic strains along sample normal direction are observed at interfaces that are approximately perpendicular to the sample normal direction. The residual elastic strains have shown gradients with maximum of $6.5\text{-}8 \times 10^{-4}$ near the graphite nodules extending into the matrix about 20 μm, where the strains are near zero. These gradients are not caused by local chemical variations.
4. The finite element modeling captures the general trend that the elastic residual strain decrease as a function of distance from the interface. However, the maximum compressive strain close to the nodule and the corresponding decreasing rate are over-predicted by a factor ~2. The main reason considered for the differences is the stress relaxation, upon the strains released by the plastic deformation of the matrix.
5. The free sample surface releases some of the compressive residual elastic stresses along the surface normal direction. The maximum residual stresses in the matrix grains are about half of the yield stress of the matrix, which suggests that the residual stresses cannot be neglected for the material fatigue properties.

Acknowledgements

Part of this work has been supported by the Strategic Research Center ‘‘REWIND -Knowledge based engineering for improved reliability of critical wind turbine components,’’ Danish Research Council for Strategic Research, grant no. 10-093966. The authors thank Profs. D Juul Jensen and N. Hansen for the helpful and stimulating discussions and for the useful comments during the preparation of the manuscript. Use of the Advanced Photon Source was supported by the U. S. Department of Energy, Office of Science, Office of Basic Energy Sciences, under Contract No. DE-AC02-06CH11357.

References

Alhussein, A., Risbet, M., Bastien, A., Chobaut, J.P., Balloy, D., Favergeon, J., 2014. Influence of silicon and addition elements on the mechanical behavior of ferritic ductile cast iron. Mater. Sci. Eng. A 605, 222–228. doi:10.1016/j.msea.2014.03.057

Andriollo, T., Thorborg, J., Tiedje, N., Hattel, J., 2016. A micro-mechanical analysis of thermo-elastic properties and local residual stresses in ductile iron based on a new anisotropic model for the graphite nodules. Model. Simulations Mater. Sci. Eng. 055012, Submitted. doi:10.1088/0965-0393/24/5/055012

Arsenault, R.J., Taya, M., 1987. Thermal residual stress in metal matrix composite. Acta Metall. 35, 651–659. doi:10.1016/0001-6160(87)90188-X

Barabash, R.I., Ice, G.E., Walker, F.J., 2003. Quantitative microdiffraction from deformed crystals with unpaired dislocations and dislocation walls. J. Appl. Phys. 93, 1457–1464. doi:10.1063/1.1534378

Barabash, R.I., Liu, W., Tischler, J.Z., Bei, H., Budai, J.D., 2012. Phase-specific elastic/plastic interface interactions in layered NiAl-Cr(Mo) structures. Acta Mater. 60, 3279–3286. doi:10.1016/j.actamat.2012.02.052

Barlow, C.Y., Hansen, N., 1991. Deformation structures and flow stress in aluminium containing short whiskers. Acta Metall. Mater. 39, 1971–1979. doi:10.1016/0956-7151(91)90166-X

Bhadeshia, H.K.D.H., David, S.A., Vitek, J.M., Reed, R.W., 1991. Stress induced transformation to bainite in pressure vessel steel. Mater. Sci. Technol. 7, 686–698. doi:10.1179/026708391790184915

Bonora, N., Ruggiero, A., 2005. Micromechanical modeling of ductile cast iron incorporating damage. Part I: Ferritic ductile cast iron. Int. J. Solids Struct. 42, 1401–1424. doi:10.1016/j.ijsolstr.2004.07.025

Chung, J.-S., Ice, G., 1999. Automated indexing for texture and strain measurement with broad-bandpass x-ray microbeams. J. Appl. Phys. 86, 5249–5255. doi:10.1063/1.371507

Dong, M.J., Tie, B., Béranger, a. S., Prioul, C., François, D., 1997. Damage Effect on the Fracture Toughness of Nodular Cast Iron. Adv. Mater. Res. 4-5, 181–188. doi:10.4028/www.scientific.net/AMR.4-5.181

Dotsenko, V.I., 1979. Stress Relaxation in Crystals. Phys. Status Solidi 11, 11–43.

Eshelby, J.D., 1957. The Determination of the Elastic Field of an Ellipsoidal Inclusion, and Related Problems. Proc. R. Soc. A Math. Phys. Eng. Sci. doi:10.1098/rspa.1957.0133

Hansen, N., 1994. Flow stress and microstructural parameters, in: 15th Risø Internaltional Symposium on Materials Science. pp. 325–334.

Hashin, Z., Shtrikman, S., 1962. A Variational approach to the theory of the elastic behaviour of polycrystals. J. Mech. Phy. Solids 10, 343–352.

Ho, S., Lavernia, E.J., 1995. Thermal residual stresses in metal matrix composites: A review. Appl. Compos. Mater. 2, 1–30. doi:10.1007/BF00567374

Huang, X., Winther, G., 2007. Dislocation structures. Part I. Grain orientation dependence. Philos. Mag. 87, 5189–5214. doi:10.1080/14786430701652851

Hütter, G., Zybell, L., Kuna, M., 2015. Micromechanisms of fracture in nodular cast iron: From experimental findings towards modeling strategies - A review. Eng. Fract. Mech. 144, 118–141. doi:10.1016/j.engfracmech.2015.06.042

Ice, G.E., Pang, J.W.L., 2009. Tutorial on x-ray microLaue diffraction. Mater. Charact. 60, 1191–1201. doi:10.1016/j.matchar.2009.07.006

Labrecque, C., Gagne, M., 1998. Review ductile iron: fifty years of continuous development. Can. Metall. Q. 37, 343–378. doi:10.1016/S0008-4433(98)00031-7

Larson, B., Yang, W., Ice, G., Budai, J., Tischler, J., 2002. Three-dimensional X-ray structural microscopy with submicrometre resolution. Nature 415, 887–890.

Larson, B.C., Levine, L.E., 2013. Submicrometre-resolution polychromatic three-dimensional X-ray microscopy. J. Appl. Crystallogr. 46, 153–164. doi:10.1107/S0021889812043737

Ledbetter, H., Austin, M., 1987. Internal strain (stress) in an SiC□Al particle-reinforced composite: an X-ray diffraction study. Mater. Sci. Eng. 89, 53–61.

Levine, L.E., Larson, B.C., Yang, W., Kassner, M.E., Tischler, J.Z., Delos-Reyes, M. a, Fields, R.J., Liu, W., 2006. X-ray microbeam measurements of individual dislocation cell elastic strains in deformed single-crystal copper. Nat. Mater. 5, 619–622. doi:10.1038/nmat1698

Liu, W., Zschack, P., Tischler, J., Ice, G., Larson, B., 2010. X-ray laue diffraction microscopy in 3D at the advanced photon source. AIP Conf. Proc. 1365, 108–111. doi:10.1063/1.3625316

Lynch, P.A., Kunz, M., Tamura, N., Barnett, M.R., 2014. Time and spatial resolution of slip and twinning in a grain embedded within a magnesium polycrystal. Acta Mater. 78, 203–212. doi:10.1016/j.actamat.2014.06.030

Ohashi, T., Barabash, R.I., Pang, J.W.L., Ice, G.E., Barabash, O.M., 2009. X-ray microdiffraction and strain gradient crystal plasticity studies of geometrically necessary dislocations near a Ni bicrystal grain boundary. Int. J. Plast. 25, 920–941. doi:10.1016/j.ijplas.2008.04.009

Poshadel, A., Dawson, P., Johnson, G., 2012. Assessment of deviatoric lattice strain uncertainty for polychromatic X-ray microdiffraction experiments. J. Synchrotron Radiat. 19, 237–244. doi:10.1107/S0909049511050400

Poulsen, H.F., Lorentzen, T., Feidenhans'L, R., Liu, Y.-L., 1997. A Synchrotron X-ray Diffraction Study of the Local Residual Strains around a Single Inclusion in an Al/W. Metal-Matrix Composite. 28, 237–243.

Theuwissen, K., Lacaze, J., Véron, M., Laffont, L., 2014. Nano-scale orientation mapping of graphite in cast irons. Mater. Charact. 95, 187–191. doi:10.1016/j.matchar.2014.06.021

Vazehrad, S., Elfsberg, J., Dioszegi, A., 2015. Study of microstructure and silicon segregation in cast iron using color etching and electron microprobe analysis. Mater. Charact. 104, 132–138. doi:10.1016/j.matchar.2014.09.008

Verdu, C., Adrien, J., Buffière, J.Y., 2008. Three-dimensional shape of the early stages of fatigue cracks nucleated in nodular cast iron. Mater. Sci. Eng. A 483-484, 402–405. doi:10.1016/j.msea.2006.09.178

Withers, P.J., Bhadeshia, H.K.D.H., 2001. Residual stress. Part 2 – Nature and origins. Mater. Sci. Technol. 17, 366–375. doi:10.1179/026708301101510087

Zhang, K.S., Bai, J.B., François, D., 1999. Ductile fracture of materials with high void volumefraction. Int. J. Solids Struct. 36, 3407–3425. doi:10.1016/S0020-7683(98)00157-7